

Article

Spatial Component Analysis to Improve Mineral Estimation Using Sentinel-2 Band Ratio: Application to a Greek Bauxite Residue

Roberto Bruno ^{1,*}, Sara Kasmaeeyazdi ^{1,*} , Francesco Tinti ¹ , Emanuele Mandanici ¹ 
and Efthymios Balomenos ²

¹ Department of Civil, Chemical, Environmental and Materials Engineering, University of Bologna, 40136 Bologna, Italy; francesco.tinti@unibo.it (F.T.); emanuele.mandanici@unibo.it (E.M.)

² Metallurgy Business Unit, MYTILINEOS S.A., Ag. Nikolaos, 320 03 Viotia, Greece; efthymios.balomenos-external@alhellas.gr

* Correspondence: roberto.bruno@unibo.it (R.B.); sara.kasmaeeyazdi2@unibo.it (S.K.); Tel.: +39-05-1209-0241 (S.K.)

Abstract: Remote sensing can be fruitfully used in the characterization of metals within stockpiles and tailings, produced from mining activities. Satellite information, in the form of band ratio, can act as an auxiliary variable, with a certain correlation with the ground primary data. In the presence of this auxiliary variable, modeled with nested structures, the spatial components without correlation can be filtered out, so that the useful correlation with ground data grows. This paper investigates the possibility to substitute in a co-kriging system, the whole band ratio information, with only the correlated components. The method has been applied over a bauxite residues case study and presents three estimation alternatives: ordinary kriging, co-kriging, component co-kriging. Results have shown how using the most correlated component reduces the estimation variance and improves the estimation results. In general terms, when a good correlation with ground samples exists, co-kriging of the satellite band-ratio Component improves the reconstruction of mineral grade distribution, thus affecting the selectivity. On the other hand, the use of the components approach exalts the distance variability.

Keywords: resources characterization; bauxite residues; band ratio; kriging of component; mineral grade



Citation: Bruno, R.; Kasmaeeyazdi, S.; Tinti, F.; Mandanici, E.; Balomenos, E. Spatial Component Analysis to Improve Mineral Estimation Using Sentinel-2 Band Ratio: Application to a Greek Bauxite Residue. *Minerals* **2021**, *11*, 549. <https://doi.org/10.3390/min11060549>

Academic Editors: Amin Beiranvand Pour, Omeid Rahmani and Mohammad Parsa

Received: 12 March 2021

Accepted: 17 May 2021

Published: 21 May 2021

Publisher's Note: MDPI stays neutral with regard to jurisdictional claims in published maps and institutional affiliations.



Copyright: © 2021 by the authors. Licensee MDPI, Basel, Switzerland. This article is an open access article distributed under the terms and conditions of the Creative Commons Attribution (CC BY) license (<https://creativecommons.org/licenses/by/4.0/>).

1. Introduction

1.1. Recovery of Minerals from Stockpiles and Tailings

Raw material and metal extractions have been conducted since pre-historic times. Mining has been present everywhere in Europe, although nowadays the majority of sites are closed. This does not mean that resources have been completely depleted. Ancient mining could not benefit from the most modern extraction and processing techniques and has left significant amounts of mining residue (including tailings and stockpiles) currently present in the territory, in the forms of semi-artificial hills, lakes, and ponds. Some of them were completely stable and never reacted with the environment, while others (especially those coming from metal mining) significantly modified the environment where they were stocked. According to “Mining and Metal in a Sustainable World 2050” [1], a major gap exists in effective retreatment technology (reuse, resize, or remove) of mining residues to meet the sustainability objectives of United Nations Development Program (UNDP) in 2030 [2].

Moreover, the depletion of the in-situ reserves, the increasing need of using lower grade materials, and advances in recovery and processing technologies are the main reasons why mining wastes are considered as recoverable resources. Moreover, the environmental

aspects have caused a strong push for more effective management of mining residuals in many mining sites [3,4]. As a first step, the raw material concentrations in tailings must be quantified and classified and a reliable expected revenue model should be developed to assess the feasibility of production, by giving particular attention to the presence of critical raw materials (CRMs) for the European Union (EU), with high impact on the economy and, at the same time, high risk of supply shortage [5,6].

A quantitative evaluation of the available resources in mining residues requires an exhaustive sampling that must be justified, so that a preliminary characterization phase is necessary for deciding if it is justified, proceeding with a full resource evaluation. Earth observation (EO) data can be useful for the abovementioned preliminary mapping and quantification of these mining residues, usually abandoned, in harsh environment, and with limited possibilities for full and fast sampling campaigns [7]. The main potentials of EO include the large number of easy to access data over large areas and their continuous acquisition over time, which may allow continuous land monitoring.

1.2. Exploitation of Remote Sensing Information

The most popular applications of satellite imagery refer to mapping problems, where the spectral content of images is used to recognize and characterize the observed surface, for instance, in terms of land cover or physical and chemical properties, among others. For these purposes, satellite images often require some kinds of geometrical and spectral calibration [8]. Before calibration, indeed, images are affected by artefacts, which depend on the sensor characteristics and the conditions at the time of acquisition, and that is to be removed to enhance the information considered useful. The general problem for mineral exploration and reserve characterization is the spatial distribution of the target variable, because, in most practical cases, in situ information is limited and sparse. Satellite images, instead, can provide dense additional information over the full area of interest, which can be used, especially when correlation is found with the in situ data.

Because of the fast and accessible information, many EO analyses have been used in mining areas and abandoned tailings, mainly for mapping pollution and environmental variables, beginning many years ago [9–13]. In the presented case studies, authors used remote sensing data and tools (such as imaging spectrometer data, and/or hyperspectral imagery combined with in situ data) to improve map accuracy of environmental pollutants affected by mining activities and their abandoned residue. In many applications, to improve map accuracy and to validate results, geostatistical approaches were used with integration of remote sensing [14–16]. The base of the geostatistical theory is the spatial correlation among georeferenced data, correlations exploitable for a correct and optimal numerical modeling of the regionalized variable (RV). Besides mapping the RV with high accuracy, as an important advantage, using geostatistical approaches provides an extra tool to improve the quality of the estimation, measured by the estimation variance maps [17]. In addition, multivariate geostatistical approaches provide an extra possibility to use more than one RV and model the correlations between RVs within so called co-regionalization modeling [18]. This analysis is able to not only verify some global results as the statistical correlations, but also to identify possible correlations between spatial components of the main variable with extra variables (the so-called secondary or auxiliary variables), including spatial anisotropies. Therefore, independent of the variables at hand (temperature, concentration, discovery probability, etc.) and of the spatial distribution model (estimation, simulation), geostatistics allow tackling the central problem: finding meaningful correlations and spatial modeling the unknown surface distribution of the interest variable, by extra information (which can be satellite data for example) [19,20].

As mentioned above, in the mining sector, while direct information is expensive, a good opportunity can be to exploit indirect information, much denser, but with good correlation with the direct variable. This is the case of the low-cost data provided by satellite images. There are many examples of mineral characterizations, where, by knowing the spectral properties of a surface feature, simple mathematical operations among spectral

bands (called band ratio) have contributed to localize outcrops and surface deposits [21–26]. To detect a specific feature or mineral, usually at least two spectral bands are necessary, one band with higher reflectance features of the given material and another one with strong absorption features for the same material [23]. There are many studies on spectral analysis of minerals based on different satellite images and specific band ratios for different minerals in a target area mainly in geological mapping [27,28]. Iron oxides are among the most studied materials using band ratio techniques [25], because of their selective absorption of light in the visible and near-infrared range caused by transitions in the electron shell [29]. For example, for detection and mapping of an iron ore formation, ferric (Fe^{3+}) and ferrous (Fe^{2+}) iron oxide specific band ratios are suggested, and thanks to their correlation with iron samples, some iron ore grades maps can be obtained [26]. Hence, the band ratio, as an appropriate index, can be considered as additional information while mapping a specific mineral of a geological feature on the surface.

This paper proposes to map the iron concentration as the strategic metal within a bauxite residue in Greece. In the first step, only direct samples from the site were used (performing ordinary kriging—OK estimation). Then, the band ratio identified for iron detection was used as additional information to map the iron variability within the bauxite residues (performing co-kriging—CK estimation). To improve the map accuracies, a new method (component co-kriging—CCK estimation) was proposed to re-construct the co-regionalization model between the sample data and the band ratio information, by exploiting the possibility of extracting a specific component from the satellite data and using it in the co-regionalization models. Finally, all three models and their results were compared to check the improvement given by the proposed model in iron estimation maps.

2. Materials and Methods

2.1. Co-Regionalization Model and Application: Current Practice

The most classical estimation method to map the spatial variability of a RV variable is OK , which uses available samples to predict in “not-available” points [17]. To add an additional variable in the kriging system, and moving into multivariate geostatistics, which in many cases improves the target variable prediction, there is a need of, at least, a second variable, with the spatial correlation among them [18]. This property can be calculated within the cross-covariance. Given two stationary random functions, $Z_1(x)$, $Z_2(x)$, with the means of m_1 and m_2 , the spatial cross-covariance $C_{12}(h) \neq C_{21}(h)$, are defined in Equation (1):

$$\begin{cases} C_{12}(h) = E[Z_1(x) \times Z_2(x+h)] - m_1 \times m_2 \\ C_{21}(h) = E[Z_2(x) \times Z_1(x+h)] - m_1 \times m_2 \end{cases} \quad (1)$$

The secondary variable can be known in all points of the domain and displaced in a regular grid. If remote sensing data are used as a secondary variable, the space-time concept should be considered because ground samples are taken in a certain time, while satellite information is repeated over time; this produces photographs of “different” stockpiles.

In this study, an iso-time framework was adopted. An image of the stockpile at the time zero (t_0) was considered, as well as all the ground samples referred to the same surface remote-sensed. Therefore, the 3D reconstruction of the distribution of concentrations is relevant to a constant time.

The objective was to map the distribution of the target variable (iron concentration as the strategic metal), using Sentinel-2 satellite data as the secondary variable. Sentinel-2 is a European satellite mission for Earth observation, which is part of the Copernicus program. It provides global coverage of multispectral imagery, composed by 13 bands in the spectral range between the visible and the short-wave infrared, with a revisiting time of five days at the equator [30]. It was selected for the present study because of the availability of the images at the date of sampling, and the good spatial resolution (pixel size from 10 to 60 m, depending on the band). Moreover, the spectral bands available in Sentinel-2 data allow the computation of different band ratios useful for mineral exploration. For iron deposits,

in particular, different band ratios were proposed in the literature for other multispectral sensors [21–26], which can also apply to Sentinel-2 images [31].

To map the iron variability, the classical steps are:

- Using one variable: iron samples, spatial variability analysis of target variable (sample variogram and its model), and finally using the OK estimation method;
- Adding extra information (as an example band ratio of iron as the secondary variable): spatial variability analysis of target variable (sample variogram and its model) and the secondary variable, the cross-correlation analysis between the target variable and the secondary variable, and finally using the CK estimation method.
- At the end, to compare the map accuracies results, cross-validation should be performed to check if adding information can improve the results.

The first approach for mapping the mineral concentration is using just the in situ samples, which in this case are represented by the mineral concentrations from the mining residues sampling. The ordinary kriging (OK) method can be used and the estimated values in all nodes of the grid can be found by using Equation (2):

$$A^{OK}(x_i) = \sum_{\alpha} \lambda_{\alpha}^{OK} \times A(x_{\alpha}) \quad (2)$$

where: $A(x_{\alpha})$ is the variable known in the points x_{α} (mineral grade from samples); λ_{α}^{OK} are the weights calculated with ordinary kriging method; $A^{OK}(x_i)$ is the estimate of the main variable in the points x_i (grid nodes).

Regarding the OK model definition, its spatial variability is object of the variogram analysis. The standard model of a stationary random function with nested structures is presented in Equation (3):

$$\gamma_A(h) = a_{nug} + \sum_u a_u \times \gamma_u(h) \quad (3)$$

where: $\gamma_A(h)$ is the variogram model of the main variable (mineral concentration from sampling); a_{nug} is the nugget effect; $\gamma_u(h)$ are the models of different nested structures (spatial components); a_u are the sills of each model component.

The second approach attempts to improve the estimation of the main variable, using the secondary (auxiliary) variable. The prerequisite is to verify if a correlation exists between two variables. The value of the correlation coefficient is defined by Equation (4):

$$\rho_{AB} = \frac{\sigma_{AB}}{\sqrt{\sigma_A^2 \times \sigma_B^2}} \quad (4)$$

where: ρ_{AB} is the correlation coefficient between the primary (mineral's grade from sampling) and secondary variable; σ_{AB} is the covariance between the primary and secondary variable; σ_A^2 is the variance of the primary variable; σ_B^2 is the variance of the secondary variable.

The CK variance allows theoretically verifying the effect of the secondary variable on reducing the estimation smoothing. The estimates by CK can be found by applying Equation (5):

$$A^{CK}(x_{i0}) = \sum_{\alpha} \lambda_{\alpha}^{CK} \times A(x_{\alpha}) + \sum_i v_i^{CK} \times B(x_i) \quad (5)$$

where: $B(x_i)$ is the auxiliary variable known in the points x_i (satellite grid nodes); λ_{α}^{CK} and v_i^{CK} are the weights for the primary and secondary variables calculated by CK; $A^{CK}(x_{i0})$ is the estimate of the main (primary) variable in the points x_{i0} one of the grid nodes.

Moreover, in the case of CK, often a linear co-regionalization model is expected (Equation (6)):

$$\begin{cases} \gamma_A(h) = a_{nug} + \sum_u a_u \times \gamma_u(h) \\ \gamma_B(h) = b_{nug} + \sum_u b_u \times \gamma_u(h) \\ \gamma_{AB}(h) = c_{nug} + \sum_u c_u \times \gamma_u(h) \end{cases} \quad (6)$$

where: $\gamma_A(h)$, $\gamma_B(h)$ are the variogram models of the first and secondary variables; $\gamma_{AB}(h)$ is cross-variogram model between the primary and the secondary variable; $\gamma_u(h)$ is the structural components of variogram models; b_{nug} is the nugget effect for the secondary variable; b_u are the sills of each component of the variogram model for the secondary variable; c_{nug} , c_u are the sills of each component for the cross-variogram model.

The comparison of estimations obtained by the OK and CK methods is performed by the following analyses [19]:

- The cross-validation;
- The estimation maps of minerals;
- The maps of estimation variance.

Usually, when the secondary variables are dense, namely available at more points than the main variable, and sufficiently correlated with the main variable, CK is typically of advantage [18].

2.2. New Perspective: Use of Spatial Components

In the case of multivariate geostatistics and in presence of a linear co-regionalization model, the selected variables (*A* as the target variable and *B* as the secondary variable) can be considered as a linear combination of independent random variables (factors) Y_{nug} , Y_i monostructure, called scale components, in addition to the mean (Equation (7)):

$$\begin{aligned} A &= m_A + \sqrt{a_{nug}} Y_{nug}^A + \sum_u \sqrt{a_u} \times Y_u^A \\ B &= m_B + \sqrt{b_{nug}} Y_{nug}^B + \sum_u \sqrt{b_u} \times Y_u^B \end{aligned} \quad (7)$$

where m_A , m_B are the means of the variables *A* and *B*; Y_{nug}^A , Y_u^A , Y_{nug}^B , Y_u^B are the structural components of the main and auxiliary variables, each of them being a {0,1} standard variable with a specific variogram structure.

The correlation coefficient between the iso-structure components of the main and auxiliary variable are presented in Equation (8):

$$\begin{aligned} \rho_{nug}^{AB} &= E[Y_{nug}^A Y_{nug}^B] \\ \rho_u^{AB} &= E[Y_u^A Y_u^B] \end{aligned} \quad (8)$$

Given the independence of factors, the total variance of the variables is just the sum of the sills of each component. Variances and covariances are presented in Equation (9):

$$\begin{cases} \sigma_A^2 = a_{nug} + \sum_u a_u \\ \sigma_B^2 = b_{nug} + \sum_u b_u \\ \sigma_{AB} = \sqrt{a_{nug} \times b_{nug} \rho_{nug}^{AB}} + \sum_u \sqrt{a_u \cdot b_u} \rho_u^{AB} = c_{nug} + \sum_u c_u \end{cases} \quad (9)$$

The correlation coefficient between the main (primary) and the secondary variable is presented in Equation (10):

$$\rho_{AB} = \frac{\sigma_{AB}}{\sqrt{\sigma_A^2 \times \sigma_B^2}} = \frac{c_{nug} + \sum_u c_u}{\sqrt{\left(a_{nug} + \sum_u a_u\right) \times \left(b_{nug} + \sum_u b_u\right)}} \quad (10)$$

In the case of having several scale components, there could be an advantage of using as auxiliary variable just one component instead of the whole initial variable. The justification for that derives by the observation that the correlation between the main and the auxiliary variables exists only at one scale (Equation (11)):

$$\rho^{AB}_{u_c} = \frac{c_{u_c}}{\sqrt{a_{u_c} \times b_{u_c}}} \rho^{AB}_{u,u' \neq u} = 0 \tag{11}$$

Such observation derives by the co-regionalization model, showing only one structure in the cross variogram, or the independence of any other structure common to the main and auxiliary variables (more generally, this approach allows also the filtering the effect of a noise [18]).

In this paper, the methodology is performed to check the improvements of the iron concentration maps, due to the increase of correlation when the auxiliary variable is just the correlated component, as shown in the following relationships (Equation (12)):

$$\begin{aligned} \sigma_{AY_{u_c}} &= E[AY_{u_c}] = \text{cov}\{AB\} = \sigma_{AB} \\ b_{u_c} &< b_{nug} + \sum_u b_u \rightarrow \sigma_{Y_{u_c}}^2 < \sigma_B^2 \\ \rho_{AY_{u_c}} &= \frac{\sigma_{AY_{u_c}}}{\sqrt{\sigma_A^2 \times \sigma_{Y_{u_c}}^2}} > \frac{\sigma_{AB}}{\sqrt{\sigma_A^2 \times \sigma_B^2}} = \rho_{AB} \end{aligned} \tag{12}$$

In terms of variograms (Equation (13)):

$$\begin{cases} \gamma_B > \gamma_{Y_{u_c}} \\ \gamma_{AB} = \gamma_{AY_{u_c}} \end{cases} \tag{13}$$

In terms of CK, using one of the components, Y_{u_c} , the estimation results are different with respect to using the original auxiliary variable B , since the new secondary variable and the weights differ from the original one. In fact, the component co-kriging system (CCK) is similar to the original CK, but with different coefficient matrix, since the submatrix of variogram of secondary variable changes (Equation (14)):

$$\begin{bmatrix} \gamma_{AA} & \gamma_{AB} & 1 & 0 \\ \gamma_{AB} & \gamma_{BB} & 0 & 1 \\ 1 & 0 & 0 & 0 \\ 0 & 1 & 0 & 0 \end{bmatrix} \neq \begin{bmatrix} \gamma_{AA} & \gamma_{AY_{u_c}} & 1 & 0 \\ \gamma_{AY_{u_c}} & \gamma_{Y_{u_c}Y_{u_c}} & 0 & 1 \\ 1 & 0 & 0 & 0 \\ 0 & 1 & 0 & 0 \end{bmatrix} \tag{14}$$

$$A^{CCK}(x_i) = \sum_a \lambda_a^{CCK} \times A(x_a) + \sum_i v_i^{CCK} \times Y_{u_c}(x_i)$$

where: $Y_{u_c}(x_i)$ is the structural component of the auxiliary variable known in the points x_i (satellite grid nodes); λ_a^{CKY} and v_i^{CCK} are the weights for the primary and auxiliary variables calculated by CCK; $A^{CCK}(x_i)$ is the estimation of the main (primary) variable in the points x_i (grid nodes).

Note that $Y^B(x_i)$ is the true component that we do not know, so that we can implement the CCK if we estimate it by factorial kriging (FK) which respects the actual data [18] in Equation (15):

$$\begin{aligned} Y_u^{FK}(x_i) &= \sum_j \lambda_j^{FK} B(x_j) \\ B &= m^{FK}_B + \sqrt{b_{nug}} Y_{nug}^{FK}(x_i) + \sum_u \sqrt{b_u} Y_u^{FK}(x_j) \end{aligned} \tag{15}$$

The second part of Equation (15) can be checked to control the estimated value of components $Y^{FK}(x_i)$. We can consider that, in case of an image band, the information is dense and the estimation quality is satisfying, so that it looks justified to use the estimated value of components in Equation (15).

The estimation variances σ^{2CK} and σ^{2CCK} allow comparing the precision of the estimations. The two estimation variances are presented in Equation (16):

$$\left\{ \begin{array}{l} \sigma_e^2(A^{CK}(x_{i0}) \rightarrow A(x_{i0})) = \sum_{\alpha} \lambda_{\alpha}^{CK} \times \gamma_A(h_{\alpha i_0}) + \mu_A^{CK} + \sum_i v_i^{CK} \times \gamma_{AY}(h_{ij_0}) + \mu_B^{CK} \\ \sigma_e^2(A^{CCK}(x_{i0}) \rightarrow A(x_{i0})) = \sum_{\alpha} \lambda_{\alpha}^{CCK} \times \gamma_A(h_{\alpha i_0}) + \mu_A^{CCK} + \sum_i v_i^{CCK} \times \gamma_{AY}(h_{ij_0}) + \mu_B^{CCK} \end{array} \right. \quad (16)$$

Moreover, to check the adopted variogram models and to check if CCK could improve the estimation results, cross-validation can be performed on data. The principle of cross-validation is to remove the target variable at each sample point x_{α} and then predict by kriging with the proposed model. Therefore, since the true values are available, it is possible to compute the kriging error [19].

2.3. Case Study: The Bauxite Residuals of Greece

Bauxite residues (BR) remained from Bayer processing of bauxite (also commonly known as “red mud”) represents important strategic wastes from mining and processing activities and they were inserted in 2020 in the list of critical raw materials for the European Union [5]. The significant amount of raw materials within these types of residues can be used as a new source of materials, specifically critical metals and rare earth elements [32]. Due to the analysis done on the BR, it has potential as a secondary resource for REE extraction [33] and TiO_2 , V_2O_5 , Al_2O_3 , Fe_2O_3 , CaO , Na_2O , SiO_2 resources.

The case study used in this research is the bauxite residue from the alumina refinery of Mytilineos S.A. in Greece, located on the Gulf of Corinth, 136 km from Athens (Figure 1). The exact location is at latitude 38.354177° and longitude 22.704671° , CRS WGS84, and its dimension is around $700 \text{ m} \times 600 \text{ m}$. Since 2006, four filter presses have been used to dewater the BR, and since 2012, all BR produced has been filter-pressed and stored as a “dry” (water content $< 26\%$) by-product in an appropriate industrial landfill [31]. Producing the dry BR is currently known as the best technique for BR materials piling, because a lower volume of deposits is stocked, with a subsequent decrease of the risk of dam failures.



Figure 1. Location of bauxite residuals (left) and a high-resolution image of daily piling materials (right).

The samples used were collected from daily accumulated materials (daily data) including the tonnage of materials with their mean concentration value, and the area in which they were piled within the BR areas from June to the end of July. The samples exact locations (coordinates) were assigned where trucks discharged their daily load of materials. Figure 2 shows the daily data during two months (June and July 2019). Therefore, since, during the two months, materials were not over-accumulating, the Sentinel 2 image selected at the end of July (date: 30 July 2019) is representative of materials during June and July (accumulated in the area from the first of June until the end of July).

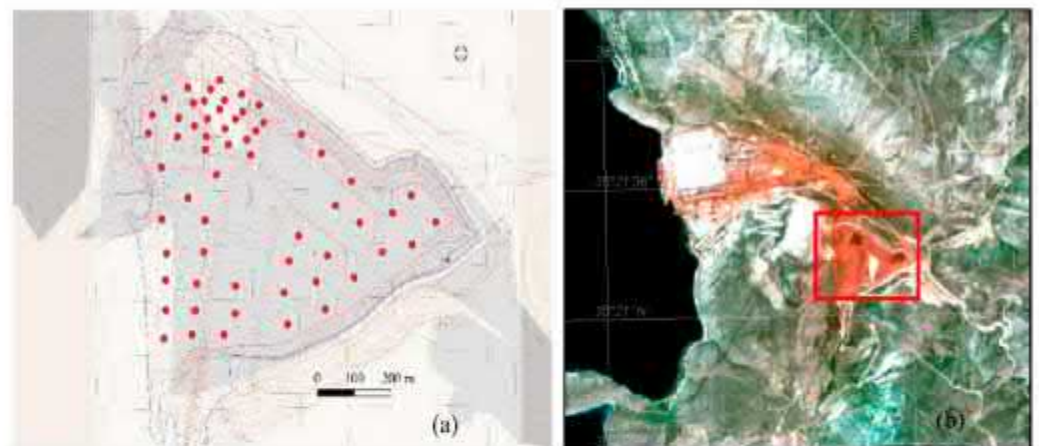


Figure 2. Samples location at the end of July 2019 (a) and Sentinel-2 true color composite image ($RGB = 4,3,2$); date: 30 July, 2019; the red line indicates the BR area (b).

The target RV selected is iron concentration Fe_2O_3 (%) as a strategic metal from samples obtained from BR of Greece. The daily samples were analyzed through X-ray fluorescence analysis-XRF, to obtain the iron concentration (Fe_2O_3 %) information at alumina refinery of Mytilineos S.A. To select the secondary variable, a preliminary test has been done to choose the most relevant band ratio (with highest correlation coefficient) for iron mapping (Table 1). Since the Sentinel-2 data are used in this study, the most common iron band ratios for identifying iron [30] have been applied. It is worthwhile to note that these ratios involve only bands at the highest spatial resolution (pixel size 10 m).

Table 1. Correlation coefficients between iron grades and band ratios of Sentinel-2 [30] at the sampling points. The highest correlation is in bold.

Band Ratios	Sentinel-2A Bands with Their Central Wavelength	Correlation Coefficient with Iron Concentration (ρ)
All iron oxides	$\frac{4 (664.9 \text{ nm})}{2 (492.1 \text{ nm})}$	−0.130
Ferrous iron oxides	$\frac{4 (664.9 \text{ nm})}{11 (1613.7 \text{ nm})}$	−0.349
Ferric Iron, Fe^{3+}	$\frac{4 (664.9 \text{ nm})}{3 (559.0 \text{ nm})}$	−0.150
Ferrous Iron, Fe^{2+}	$\frac{12 (2202.4 \text{ nm})}{8 (832.8 \text{ nm})} + \frac{3 (559.0 \text{ nm})}{4 (664.9 \text{ nm})}$	0.194
Ferrous silicates	$\frac{12 (2202.4 \text{ nm})}{11 (1613.7 \text{ nm})}$	−0.125
Ferric oxides	$\frac{11 (1613.7 \text{ nm})}{8 (832.8 \text{ nm})}$	0.223

From the presented correlation coefficients between iron concentration and band-ratios (Table 1), the one with the highest correlation (ferrous iron oxides: 4/11) is chosen as the secondary variable to map the iron concentration variability within the BR.

The histogram of iron concentration samples and the correlation between the selected band ratios (ferrous iron oxides (4/11) band ratio) is exposed in Figure 3.

Band data are extracted from the Sentinel-2 image (see Figure 2) only inside the boundaries of the BR area. The base map of the extracted band ratio values and the histogram of data are shown in Figure 4.

Considering the iron concentration as the target variable and the ferrous iron oxides band ratio as the secondary variable, it is possible, first, to map the iron variability in BR using only iron samples. Secondly, it is possible to check if map accuracies can be improved by adding the band ratio variable. Finally, by decomposition of the band ratio variable, in the case of higher correlation, using one component can improve the iron estimation maps.

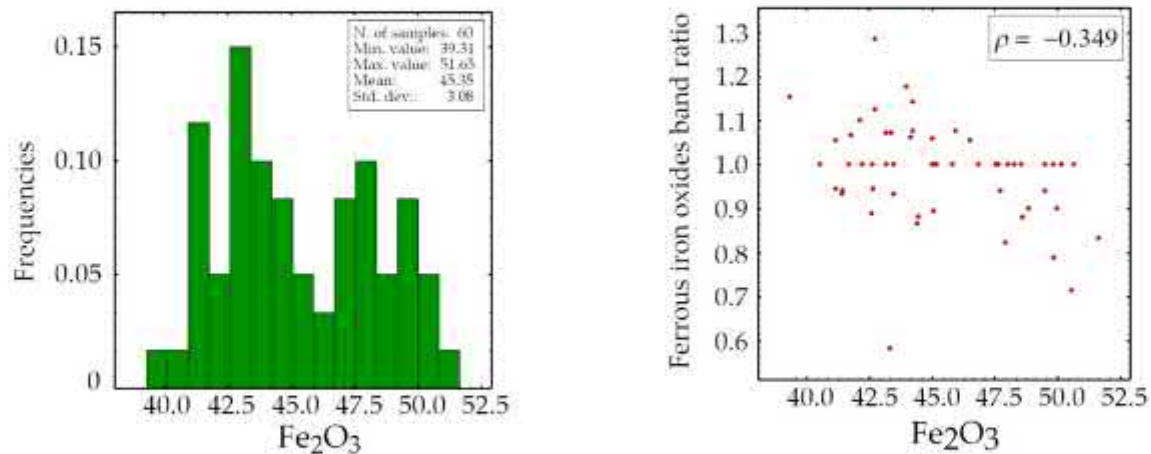


Figure 3. Histogram of Fe₂O₃ (%) of samples (left) and correlation with band ratio ferrous iron oxides: Band4/Band11 (right).

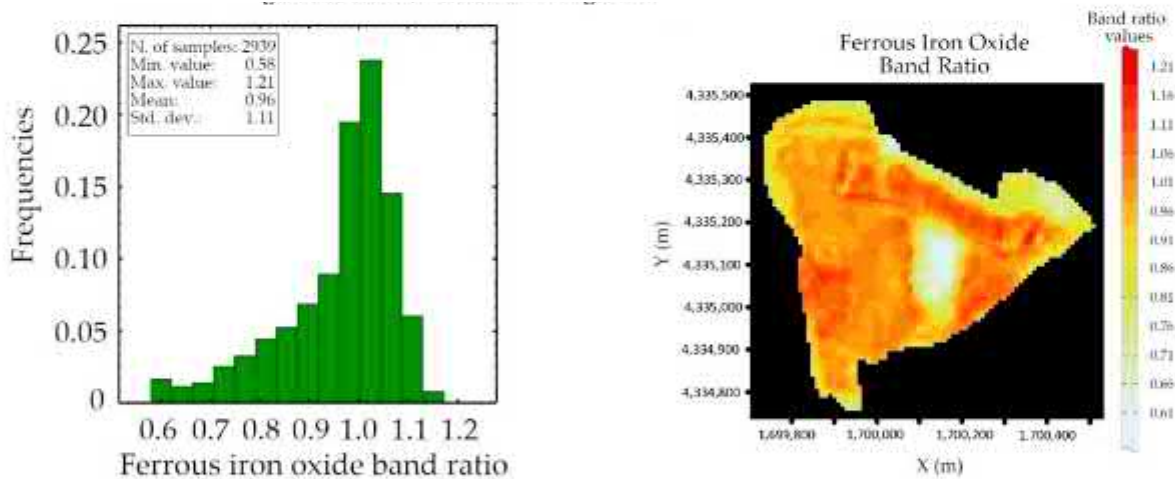


Figure 4. Histogram of ferrous iron oxides band ratio (left) and its base map (right).

3. Results

In the first step, using only iron samples, to perform OK, the sample variogram and variogram model is shown in Figure 5, including two spherical structures. The red bars below the variogram show the frequency of sample pairs used in variogram calculations. The variogram model parameters are presented in Table 2.

Table 2. Structures and parameters of variogram models fitted on Fe₂O₃ (%) samples variogram.

Fe ₂ O ₃ (%) Variogram Models				
Nugget Effect	Spherical 1		Spherical 2	
	Range (m)	Sill	Range (m)	Sill
2.3	70	2.9	180	3.4

Using the variogram model of Figure 5, it is possible to perform OK. Maps of Fe₂O₃ (%) concentration variability and estimation standard deviation are presented in Figure 6.

To improve the iron estimation results, in the second step, the presented secondary variable (the ferrous iron oxides (4/11) band ratio) can be added to map the iron concentration variability.

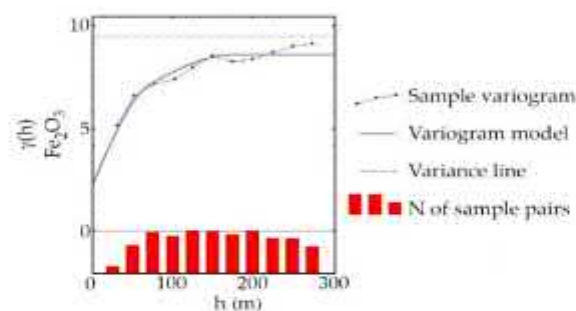


Figure 5. Sample variogram and variogram model for iron concentration obtained by samples Fe_2O_3 (%). $h(m)$ is the distance and $\gamma(h)$ is the sample variogram.

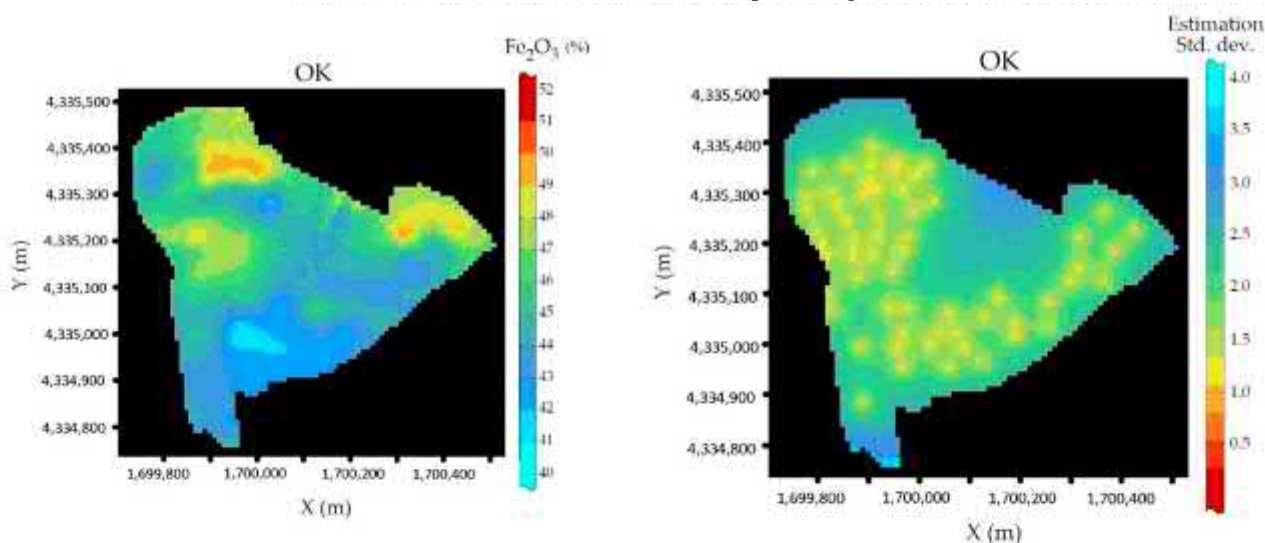


Figure 6. Fe_2O_3 (%) estimated map (OK) (left) and the estimation variance map (right) by performing OK.

To perform co-kriging, the sample variograms and variogram models considering both variables (iron as main variable and ferrous iron oxides band ratio as the secondary variable) and cross variogram are calculated and shown in Figure 7. The fitted model for iron concentration is equal to the model used in OK. Using the same model makes the comparisons more logical between the OK and CK. The structure and model details are presented in Table 3.

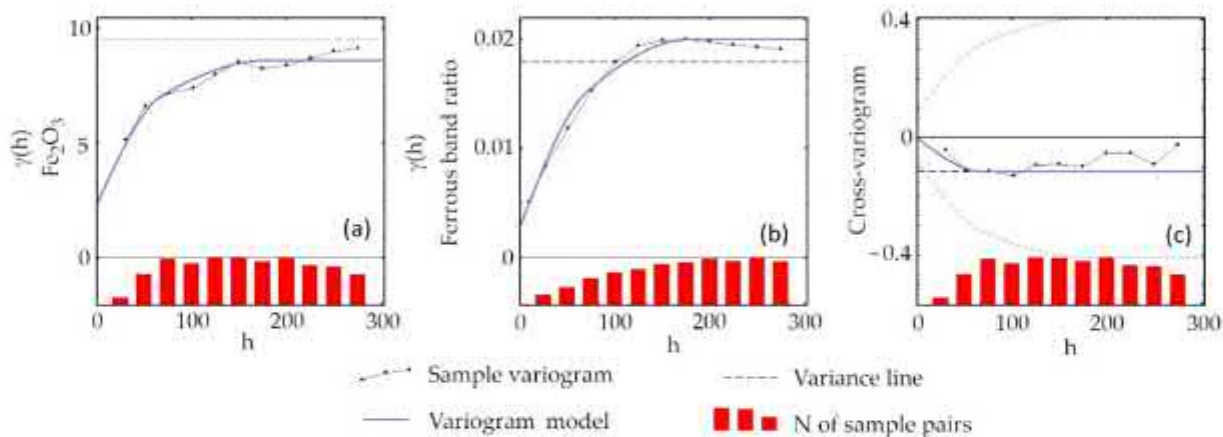
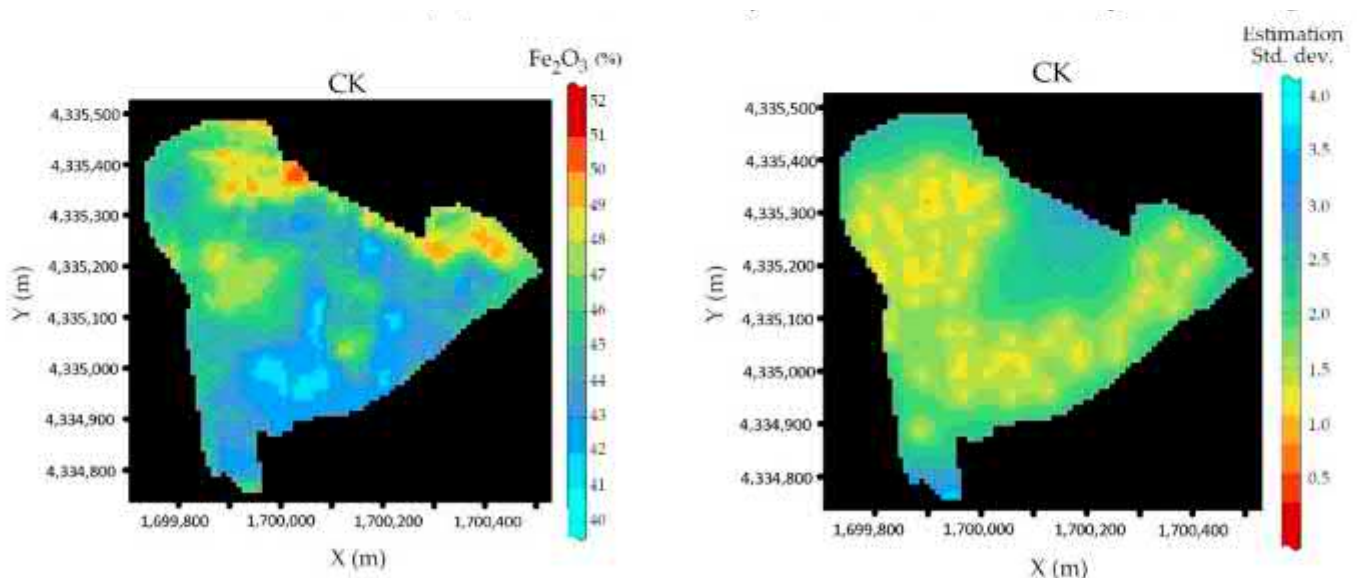


Figure 7. Sample variograms and variogram models for iron concentration obtained by samples Fe_2O_3 (%) (a), ferrous iron oxides band ratio (b) and cross-variogram (c). $h(m)$ is the distance and $\gamma(h)$ is the sample variogram.

Table 3. Structures and parameters of variogram models fitted on Fe_2O_3 (%) samples, ferrous iron oxides band ratio, and cross-variogram.

Direct variable— Fe_2O_3 (%)—Variogram Models				
Nugget Effect	Spherical 1		Spherical 2	
	Range (m)	Sill	Range (m)	Sill
2.3	70	2.9	180	3.4
Auxiliary Variable—Band Ratio—Variogram Models				
Nugget Effect	Spherical 1		Spherical 2	
	Range (m)	Sill	Range (m)	Sill
0.0027	70	0.0063	180	0.011
Cross-Variogram Models				
Nugget Effect	Spherical 1		Spherical 2	
	Range (m)	Sill	Range (m)	Sill
0	70	−0.116	180	0.0001

Using the presented variogram models of Figure 7, it is possible to perform CK. Maps of Fe_2O_3 (%) concentration variability and estimation variance are presented in Figure 8.

**Figure 8.** Fe_2O_3 (%) estimated map (CK) (left) and the estimation variance map (right) by performing co-kriging between samples and ferrous iron oxide band ratio.

Finally, the new approach was performed by decomposition of the secondary variable (the ferrous iron oxide band ratio).

In the first step, to choose the appropriate component, the correlation coefficients are calculated, using the variogram models' structures, and due to Equation (9):

$$\begin{aligned}
 \gamma_{iron} &= 2.3 + 2.9 \times \gamma(R = 70) + 3.4 \times \gamma(R = 180) \\
 \gamma_{ferrous.iron.band.ratio} &= 0.0027 + 0.0063 \times \gamma(R = 70) + 0.011 \times \gamma(R = 180) \\
 \gamma_{cross.variogram} &= -0.116 \times \gamma(R = 70) + 0.0001 \times \gamma(R = 180)
 \end{aligned} \quad (17)$$

Hence, the correlation coefficient between components of ferrous iron oxides band ratio and iron concentration can be calculated as bellow:

$$\begin{aligned}
 \sigma_A &= 2.3 + 2.9 + 3.4 = 8.6 \\
 \sigma_B &= 0.0027 + 0.0063 + 0.011 = 0.02 \\
 \sigma_{AB} &= 0 - 0.116 + 0.0001 = -0.1159 \\
 \sigma_{component1} &= \sigma_{Y1} = 0.0063 \\
 \sigma_{component2} &= \sigma_{Y2} = 0.011
 \end{aligned}
 \tag{18}$$

Two components are related to the small range ($R = 70$ m) and the large range ($R = 180$). Therefore, it is possible to calculate the correlation coefficients:

$$\begin{aligned}
 \rho_{A/B} &= \frac{\sigma_{AB}}{\sqrt{\sigma_A^2 \times \sigma_B^2}} = \frac{-0.1159}{\sqrt{8.6 \times 0.02}} = -0.279 \\
 \rho_{A/Y1} &= \frac{\sigma_{AY1}}{\sqrt{\sigma_A^2 \times \sigma_{Y1}^2}} = \frac{-0.116}{\sqrt{8.6 \times 0.0063}} = -0.498 \\
 \rho_{A/Y2} &= \frac{\sigma_{AY2}}{\sqrt{\sigma_A^2 \times \sigma_{Y2}^2}} = \frac{0.0001}{\sqrt{8.6 \times 0.011}} = 0.0003 \\
 \rho_{A/Y1} &= -0.498 > 0.279 = \rho_{A/B}
 \end{aligned}
 \tag{19}$$

Since the first component has the highest correlation coefficient (negative correlation) with iron concentration, it is selected as the appropriate component to test the CCK.

In this step, to use the selected component in Equation (13), there is a need of estimating the component in all points of the grid. To do it, the CK is performed on band-ratio data, using only the first structure of the variogram model. To check the coherency of results from Equation (15), the estimated maps of both components (small range, $R = 70$ m, and large range, $R = 180$ m), plus the estimated mean are shown in Figure 9.

The sum of three maps (estimated components and mean estimated) is equal to the original values of ferrous iron oxides band ratio as Equation (15).

The small range component ($R = 70$ m) as having the higher coefficient correlation can be used as the secondary variable to perform CCK.

The parameters of variogram models are shown in Table 4. The same as CK, the fitted model on target variable (iron concentration) is equal to the previous models.

Table 4. Main parameters of the variogram model from Fe_2O_3 (%) of samples, first component of ferrous iron oxides band ratio and cross-variogram.

Nugget Effect	Fe ₂ O ₃ (%) Variogram Models			
	Spherical 1		Spherical 2	
	Range (m)	Sill	Range (m)	Sill
2.3	70	2.9	180	3.4
	Band Ratio-Component 1 Variogram Models			
	Spherical 1			
	Range (m)		Sill	
	70		0.0063	
	Cross-Variogram Models			
	Spherical 1			
	Range (m)		Sill	
	70		-0.116	

Maps of Fe_2O_3 (%) concentration using CCK method and its estimation variances are presented in Figure 10.

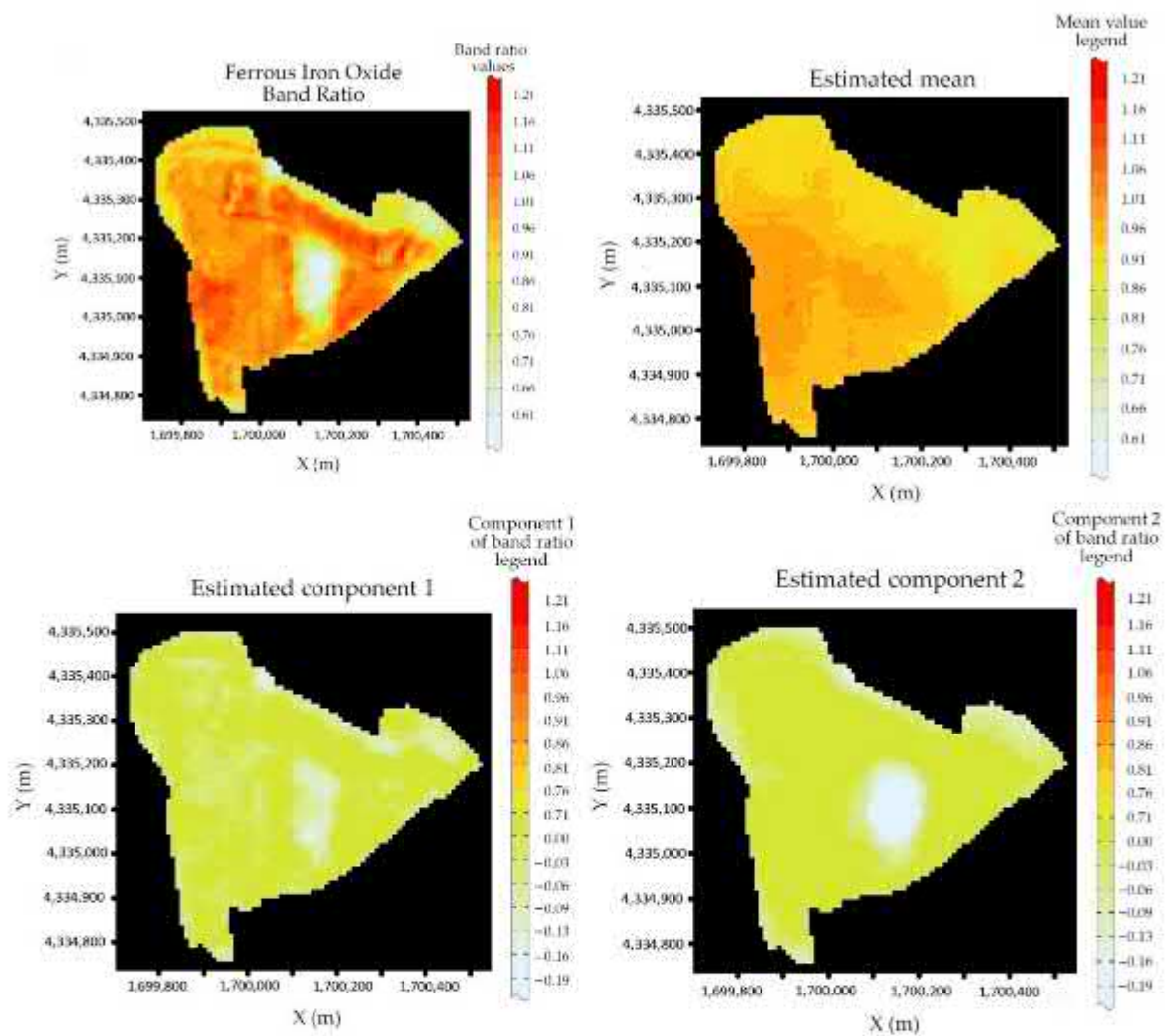


Figure 9. Base maps of real data values of ferrous iron oxides band ratios (**upper left**) and estimated components: small range component (**lower left**) and large range component (**lower right**), and the mean estimation map (**upper right**), all deposited from ferrous iron oxides band ratios.

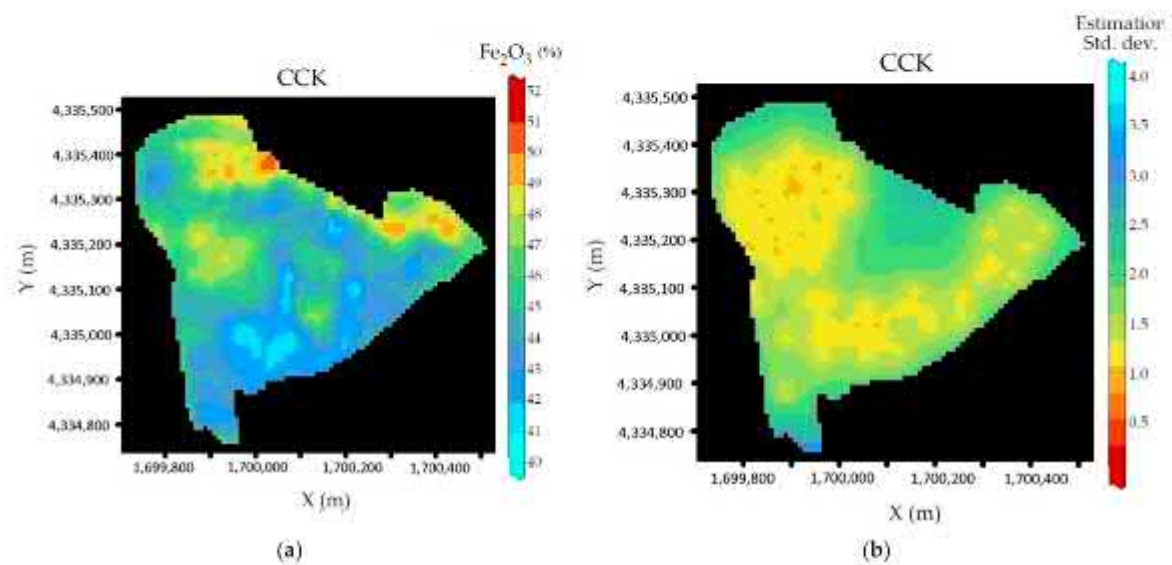


Figure 10. Fe_2O_3 (%) estimated map (CCK) (a) and the estimation variance map (b), by performing CCK between iron samples and the first component of ferrous iron oxide band ratio (Range = 70 m).

Finally, Figure 11 shows the main statistics of the cross-validation for three solutions, OK, CK, and CCK. Cross-validation performed by removing sample values (one-by-one) and estimating them using the selected model and neighborhood for three methods (OK, CK, and CCK). The scatter plots between estimated and true values of Fe_2O_3 (%) at 60 sample points, standardized estimation error, and scatter plot between error and estimated values are compared for all three solutions.

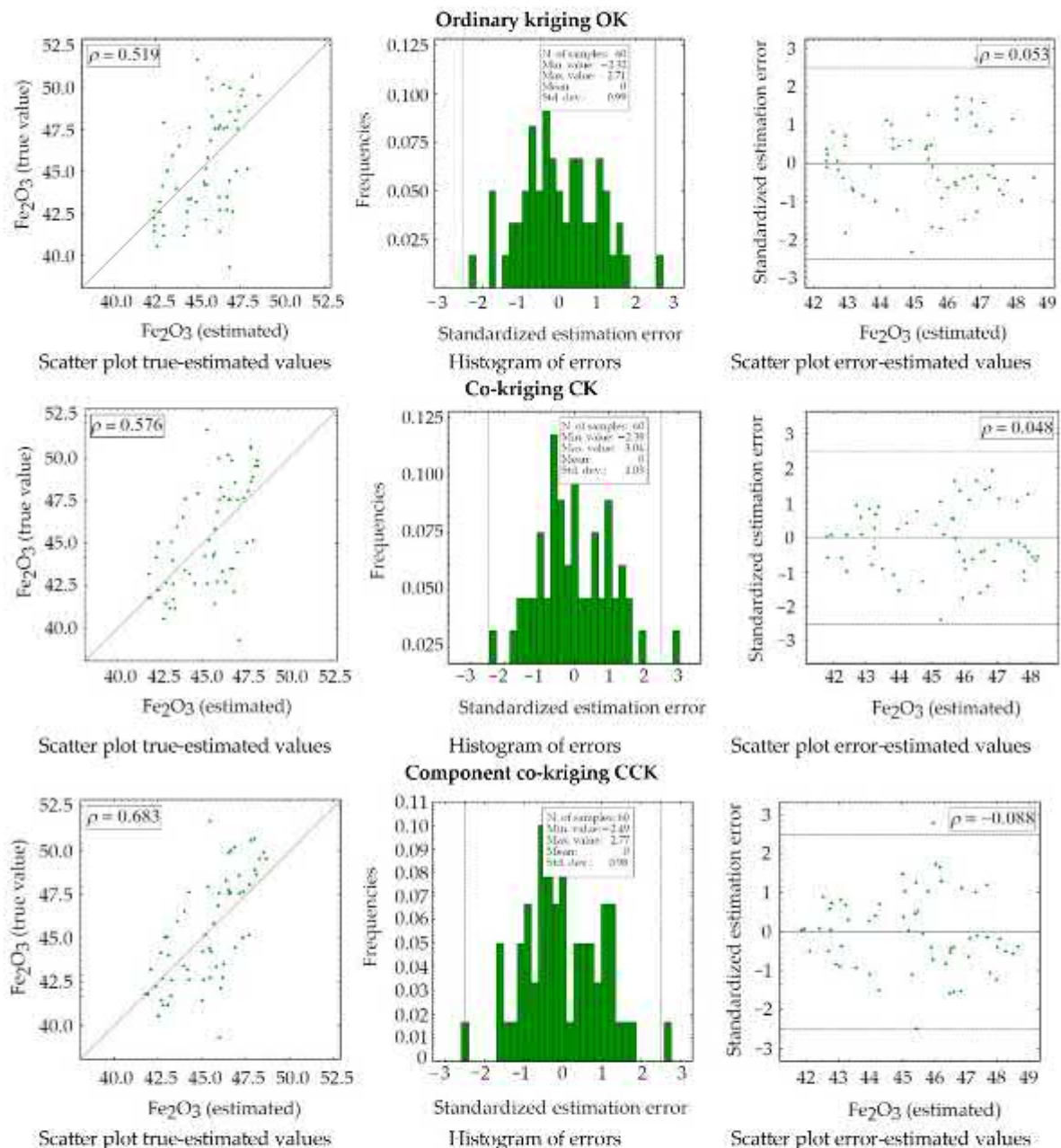


Figure 11. Statistics of cross-validation for OK, CK, and CCK results: scatter plot between true values of Fe_2O_3 (%) at 60 sample points and estimated values (left), standardized estimation error (center), and scatter plot between error and estimated values (right).

4. Discussion

Mapping a metal distribution within an artificial resource, such as a mining waste area is quite challenging and complex. Therefore, there are not many examples of using geostatistical methods for tailings characterization. Some researchers tried to map metal variability within mine tailings using in field samples and performed ordinary kriging.

However, they faced with the challenge of a small number of samples while performing geostatistical modeling [34]. Another example is characterizing the mining residues using geostatistical co-kriging estimation [35,36]. In both examples, the traditional co-kriging method is used. However, an efficient estimation of metal variability is essential, since all economic evaluations are based on metals variability maps and estimation. Therefore, the higher accuracy of the map can make the difference, when deciding whether the exploitation of a strategical resource is economically feasible and sustainable. Iron maps variability as the main target in this work is focused within a bauxite residue in Greece. Most classical estimation method of *OK* is performed and estimation map has shown mainly three high grade parts (more than 50% of Fe_2O_3) in north east and south east of *BR*. The estimation standard deviation map identified the lowest estimation variance at the samples points and a high variation where the number of samples are low (east and middle part of the *BR*).

By adding *EO* data and specifically Sentinel-2 image (a free and easily accessible image) at the date of sampling, the improvement of iron mapping was tested. The ferrous iron oxides band ratio was selected as the secondary variable to see if additional information (in a regular grid at all estimation points) can help the iron estimation mapping. Results of *CK* has shown a higher variability with more anomaly points (with Fe_2O_3 concentration of more than 50%) in the estimation map. Moreover, adding the band ratio data could decrease the variability and the values of the estimation variance map. Finally, the new hypothesis of using the most correlated component was tested. Due to the co-regionalization structures, it was possible to decompose the band ratio values into mean, nugget effect, and two different range components: a small range component (70 m) and a large range component (180 m).

The correlation coefficient between each component and iron was calculated and the first component with the small range (70 m) was selected due to its higher correlation with iron. To use this component in the *CK* system, there was a need to estimate it for all grid points, and then the estimated component was used to perform *CCK*. The appropriate check was done to control the equality of Equation (13). In Figure 9, by mathematically summing at each grid node, the values of all three maps (estimated component 1 and 2 and the estimated mean), the original map of the ferrous iron oxides band ratio is obtained. This mathematical check confirms that the estimated component 1 can be used in the *CCK* estimation based on Equation (15).

To do the comparisons among the three utilized methods (*OK*, *CK*, and *CCK*), in all three estimations, the iron variogram model is the same. Moreover, the neighborhoods used for estimations were equal, to have the same condition, while mapping the iron variability.

At the end, the cross-validation was performed to check the efficiency of three methods. For the scatter plots between the true and estimated values of iron (Fe_2O_3) at sample points, the higher correlation between the estimated values and true values is related to the *CCK*, with $\rho = 0.68$. The histogram of the standardized estimation errors provides an idea about the unbiasedness and also the quality of the estimate. It also helps locate the outliers, which are outside the two vertical lines corresponding to the threshold value. In all three methods, the mean of the histogram is close to zero and shows the acceptable estimation results. Then the scatter plot of the standardized estimation errors versus the estimated values is calculated, which should be with no preferential shape. The reason is the independency of the standardized error with the estimated values. Since the two variables are theoretically independent, this cloud should have no preferential shape, and this was confirmed by the low correlation coefficients calculated.

5. Conclusions

Mapping the strategic metals is one of the most delicate phases, and by using satellite images, an important improvement in the model quality of surface distribution can be performed. Geostatistical models offer a wide variety of powerful tools for a deep study of metals mapping and estimations. A strategic case study (a bauxite mining residue)

is reported as an example to check the best method for mapping the iron concentration ($Fe_2O_3\%$). The proposed method of component co-kriging highlights not only the best secondary variable for iron estimation (with higher correlation coefficient), but also improves the classical ordinary-kriging and co-kriging estimation maps. The cross-validation results confirm the improvements of the results. Hence, to sum up:

- Remote sensing data are essential when mapping a surface feature, such as mapping the iron concentration variability;
- Band ratio can be considered an important auxiliary variable in geostatistical modeling, when there is correlation between in field samples and band ratios;
- Component co-kriging is an efficient method and, in case of high correlation coefficient between one component of the auxiliary variable and the main variable (in this work, the iron concentration), it can substantially improve the mapping results.

Author Contributions: Data curation, S.K., F.T. and E.M.; Investigation, R.B.; Methodology, R.B. and S.K.; Resources, E.B.; Writing—original draft, S.K. and F.T.; Writing—review & editing, R.B., S.K., F.T., E.M. and E.B. All authors have read and agreed to the published version of the manuscript.

Funding: This research was supported by the RawMatCop Programme (2018–2021), funded by the European Commission and EIT RawMaterials, grant agreement number 271/G/Gro/COPE/17/10036” and by the INCO-Piles 2020 Project (2020–2021), funded by EIT RawMaterials, Grant Agreement 19169.

Data Availability Statement: Not applicable.

Acknowledgments: The authors would like to thank Irene Benito Rodríguez, the RawMatCop Programme manager, Fabio Ferri, the INCO-Piles 2020 Project Officer, and Rima Dapous and Wesley Crock, all from EIT RawMaterials. Moreover, the authors would like to thank Dimitrios Panias from the National Technical University of Athens and Panagiotis Davris from Mytilineos S.A., for their support during the field trip and data access for the case study.

Conflicts of Interest: The authors declare no conflict of interest.

References

1. World Economic Forum (2005) Mining & Metals in a Sustainable World 2050, Ind Agenda. Available online: <https://www.weforum.org/press/2015/09/mining-and-metals-in-a-sustainable-world-2050-report-launch/> (accessed on 20 May 2021).
2. UN General Assembly (2015) Transforming Our World: The 2030 Agenda for Sustainable Development 21 October 2015. A/RES/70/1. Available online: <https://www.refworld.org/docid/57b6e3e44.html> (accessed on 20 May 2021).
3. Lebre, E.; Corder, G.D.; Golev, A. The role of the mining industry in a circular economy—A framework for resource management at the mine site level. *J. Ind. Ecol.* **2017**, *21*, 662–672. [CrossRef]
4. Mancini, L.; Sala, S. Social impact assessment in the mining sector: Review and comparison of indicators frameworks. *Resour. Policy* **2018**, *57*, 98–111. [CrossRef]
5. COM (2020) 474 Final Communication from the Commission to the European Parliament, the Council, the European Economic and Social Committee and the Committee of the Regions Critical Raw Materials Resilience: Charting a Path towards Greater Security and Sustainability. Available online: <https://eur-lex.europa.eu/legal-content/EN/TXT/?uri=CELEX%3A52020DC0474> (accessed on 20 May 2021).
6. Ferro, P.; Bonollo, F. Materials selection in a critical raw materials perspective. *Mater. Des.* **2019**, *177*, 107848. [CrossRef]
7. Jutz, S.; Milagro-Perez, M. Copernicus Program. *Compr. Remote Sens.* **2017**, *1*, 150–191. [CrossRef]
8. Follador, M. Using remote sensing for mineral characterization in tropical forest areas of Brazil, GIS and Spatial Analysis. In *2005 Annual Conference of the International Association for Mathematical Geology*; IAMG: Fortaleza, Brazil, 2005; pp. 127–132, ISBN 0973422017.
9. Ferrier, G. Application of imaging spectrometer data in identifying environmental pollution caused by mining at Rodaquilar, Spain. *Remote Sens. Environ.* **1999**, *68*, 125–137. [CrossRef]
10. Mars, J.C.; Crowley, J.K. Mapping mine wastes and analyzing areas affected by selenium-rich water runoff in southeast Idaho using AVIRIS imagery and digital elevation data. *Remote Sens. Environ.* **2003**, *84*, 422–436. [CrossRef]
11. Choe, E.; Van der Meer, F.; Van Ruitenbeek, F.; Van der Werff, H.; Boudewijn de Smeth, B.; Kim, K.W. Mapping of heavy metal pollution in stream sediments using combined geochemistry, field spectroscopy, and hyperspectral remote sensing: A case study of the Rodalquilar mining area, SE Spain. *Remote Sens. Environ.* **2008**, *112*, 3222–3233. [CrossRef]
12. Pascucci, S.; Belviso, C.; Cavalli, R.M.; Palombo, A.; Pignatti, S.; Santini, F. Using imaging spectroscopy to map red mud dust waste: The Podgorica aluminum complex case study. *Remote Sens. Environ.* **2012**, *123*, 139–154. [CrossRef]

13. Werner, T.T.; Bebbington, A.; Gregory, G. Assessing impacts of mining: Recent contributions from GIS and remote sensing. *Extr. Ind. Soc.* **2019**, *6*, 993–1012. [[CrossRef](#)]
14. Lopez-Granados, F.; Jurado-Exposito, M.; Pena-Barragan, J.M.; Garcia-Torres, L. Using geostatistical and remote sensing approaches for mapping soil properties. *Eur. J. Agron.* **2005**. [[CrossRef](#)]
15. Liu, Y.; Cao, G.; Zhao, N.; Mulligan, K.; Ye, X. Improve ground-level PM2.5 concentration mapping using a random forests-based geostatistical approach. *Environ. Pollut.* **2018**. [[CrossRef](#)]
16. Bzdęga, K.; Zarychta, A.; Urbisz, A.; Szporak-Wasilewska, S.; Ludynia, M.; Fojcik, B.; Tokarska-Guzik, B. Geostatistical models with the use of hyperspectral data and seasonal variation—A new approach for evaluating the risk posed by invasive plants. *Ecol. Indic.* **2021**. [[CrossRef](#)]
17. Matheron, G. The intrinsic random functions and their applications. *Adv. Appl. Probab.* **1973**, *5*, 439–468. [[CrossRef](#)]
18. Wackernagel, H. Multivariate Geostatistics. In *An Introduction with Applications*; Springer: Heidelberg/Berlin, Germany, 2003; pp. 121–208. [[CrossRef](#)]
19. Chiles, J.P.; Delfiner, P. *Geostatistics Modeling Spatial Uncertainty*, 2th ed.; Wiley: Hoboken, NJ, USA, 2012; pp. 118–177, ISBN 978-0-470-18315-1.
20. Van der Meer, F. Extraction of mineral absorption features from high-spectral resolution data using non-parametric geostatistical techniques. *Int. J. Remote Sens.* **1994**, *15*, 2193–2214. [[CrossRef](#)]
21. Yamaguchi, Y.; Kahle, A.B.; Tsu, H.; Kawakami, T.; Pniel, M. Overview of Advanced Spaceborne Thermal Emission and Reflection Radiometer (ASTER). *IEEE Trans. Geosci. Remote Sens.* **1998**, *36*, 1062–1071. [[CrossRef](#)]
22. Yamaguchi, Y.; Fujisada, H.; Tsu, H.; Sato, I.; Watanabe, H.; Kato, M.; Kudoh, M.; Kahle, A.B.; Pniel, M. ASTER early image evaluation. *Adv. Space Res.* **2001**, *28*, 69–76. [[CrossRef](#)]
23. Rouskov, K.; Popov, K.; Stanislav Stoykov, S.; Yamaguchi, Y. Some applications of the remote sensing in geology by using of ASTER images. In Proceedings of the Scientific Conference “SPACE ECOLOGY SAFETY” with International Participation, Sofia, Bulgaria, 10–13 June 2005.
24. de Morais, M.C.; Martins Junior, P.P.; Paradella, W.R. Multi-scale approach using remote sensing images to characterize the iron deposit N1 influence areas in Carajás Mineral Province (Brazilian Amazon). *Environ. Earth Sci.* **2012**, *66*, 2085–2096. [[CrossRef](#)]
25. Van der Meer, F.D.; Van der Werff, H.M.A.; Van Ruitenbeek, F.J.A.; Hecker, C.A.; Bakker, W.H.; Noomen, M.F.; Van der Meijde, M.; Carranza, E.J.M.; de Smeth, J.B.; Woldai, T. Multi- and hyperspectral geologic remote sensing: A review. *Int. J. Appl. Earth Obs.* **2012**, *14*, 112–128. [[CrossRef](#)]
26. Gopinathan, P.; Parthiban, S.; Magendran, T.; Al-Quraishi, A.M.; Singh, A.K.; Singh, P.K. Mapping of ferric (Fe³⁺) and ferrous (Fe²⁺) iron oxides distribution using band ratio techniques with ASTER data and geochemistry of Kanjamalai and Godumalai, Tamil Nadu, south India. *Remote Sens. Appl. Soc. Environ.* **2020**, *18*, 100306. [[CrossRef](#)]
27. Guha, A.; Singh, V.K.; Parveen, R.; Vinod Kumar, K.; Jeyaseelan, A.T.; Dhanamjaya Rao, E.N. Analysis of ASTER data for mapping bauxite rich pockets within high altitude lateritic bauxite, Jharkhand, India. *Int. J. Appl. Earth Obs. Geoinf.* **2013**, *21*, 184–194. [[CrossRef](#)]
28. Krishnamurthy, Y.V.N.; Sreenivasan, G. Remote Sensing Technology for Exploration of Mineral Deposits with Special Reference to Bauxite and Related Minerals. In Proceedings of the 16th International Symposium of ICSOBA, “Status of Bauxite Alumina, Aluminium, Downstream Products and Future Prospects”, Nagpur, India, 28–30 November 2005; pp. 68–83.
29. Ben Dor, E.; Irons, J.R.; Epema, G.F. Soil Reflectance. In *Remote Sensing for the Earth Sciences: Manual of Remote Sensing*, 3rd ed.; Rencz, A.N., Ryerson, R.A., Eds.; John Wiley & Sons: New York, NY, USA, 1999; Volume 3, pp. 111–173.
30. Drusch, M.; Del Bello, U.; Carlier, S.; Colin, O.; Fernandez, V.; Gascon, F.; Hoersch, B.; Isola, C.; Laberinti, P.; Martimort, P.; et al. Sentinel-2: ESA’s Optical High-Resolution Mission for GMES Operational Services. *Remote Sens. Environ.* **2012**, *120*, 25–36. [[CrossRef](#)]
31. Van der Werff, H.; Van der Meer, F. Sentinel-2A MSI and Landsat 8 OLI Provide Data Continuity for Geological Remote Sensing. *Remote Sens.* **2016**, *8*, 883. [[CrossRef](#)]
32. Balomenos, E.; Davris, P.; Pontikes, Y.; Pnias, D.; Delipaltas, A. Bauxite residue handling practice and valorisation research in Aluminium of Greece. In: Pontikes Y (ed) Proceedings of Bauxite residue valorization and best practices conference. *Athens* **2018**, *7*, 27–36.
33. Davris, P.; Balomenos, E.; Pnias, D.; Paspaliaris, I. Selective leaching of rare earth elements from bauxite residue (red mud), using a functionalized hydrophobic ionic liquid. *Hydrometallurgy* **2016**, *164*, 125–135. [[CrossRef](#)]
34. Candeias, C.; F Ávila, P.F.; Ferreira da Silva, E.; Paulo Teixeira, J. Integrated approach to assess the environmental impact of mining activities: Estimation of the spatial distribution of soil contamination (Panasqueira mining area, Central Portugal). *Environ. Monit. Assess.* **2015**, *187*, 135. [[CrossRef](#)]
35. Kasmaee, S.; Tinti, F.; Bruno, R. Characterization of metal grades in a stockpile of an iron mine (case study- Choghart iron mine, Iran). *Rud. Geol. Naft. Zb.* **2018**, *33*, 51–59. [[CrossRef](#)]
36. Kasmaeeyazdi, S.; Mandanici, E.; Balomenos, E.; Tinti, F.; Bonduà, S.; Bruno, R. Mapping of Aluminum Concentration in Bauxite Mining Residues Using Sentinel-2 Imagery. *Remote Sens.* **2021**, *13*, 1517. [[CrossRef](#)]